International Journal of Pharmaceutics 664 (2024) 124620

Contents lists available at ScienceDirect

International Journal of Pharmaceutics

journal homepage: www.elsevier.com/locate/ijpharm

Modelling insertion behaviour of PVP (Polyvinylpyrrolidone) and PVA (Polyvinyl Alcohol) microneedles

M. Soorani [a], Q.K. Anjani [b], E. Larrañeta [b], R.F. Donnelly [b], D.B. Das [a,*]

[a] Department of Chemical Engineering, Loughborough University, Loughborough, LE11 3TU, United Kingdom
[b] School of Pharmacy, Queen's University Belfast, Medical Biology, 97 Lisburn Road, Belfast, BT9 7BL, United Kingdom

ARTICLE INFO

Keywords:
Microneedle materials
Skin non-linearity
Ramberg–Osgood model
Computer simulation
PVP/PVA microneedle
Laser-engineered silicone micromould

ABSTRACT

A comprehensive investigation into the effects of nonlinear material behaviour of polymeric (MN) and skin on the dynamics of the MN insertion in skin was undertaken in this study using experiments and numerical simulations. The nonlinearity of the material behaviour was incorporated by employing the Ramberg–Osgood and neo-Hookean equations for stress–strain relationships for the MN materials and skin, respectively. For this purpose, a characteristic type of dissolving MN array was selected. This type of MN is made by a combination of poly(vinyl alcohol) and poly(vinyl pyrrolidone). The numerical simulations were validated using experimental investigations where the MNs were fabricated using laser-engineered silicone micromould templates technology. Young's modulus, Poisson's ratio, and compression breaking force for the MN polymers were determined using a texture analyser. The alignment between experimental findings and simulation data underscores the accuracy of the parameters determined through mechanical testing and mathematical calculations for both MN materials (PVP/PVA) and skin behaviour during the MN insertion. This study has demonstrated a strong alignment between the experimental findings and computational simulations, confirming the accuracy of the established parameters for MNs and skin interactions for modelling MN insertion behaviour in skin, providing a solid foundation for future research in this area.

1. Introduction

The effectiveness of microneedle (MN) systems is closely tied to their penetration depth, a factor that previous studies have shown to influence their ability to deliver therapeutic agents (De Martino et al., 2022; Chang et al., 2021; Makvandi et al., 2021a). This is especially important for MNs containing their drug cargo located within the needle, such as dissolving and coated MN arrays (Xiu et al., 2022; Larrañeta et al., 2016; Ang et al., 2020). Despite the recognised importance of skin penetration for drug delivery (Aldawood et al., 2021), current MN research has primarily relied on attempts to fabricate various MN systems and related experimental studies, often neglecting the crucial role that mathematical modelling can play in modelling and optimising their performances, such as the penetration depths.

Understanding the dynamics of MN penetration in the skin is essential for enhancing MN design and maximising their therapeutic impacts, making it a critical step in developing more effective MN arrays for the future. This is especially important considering that measuring the MN insertion accurately requires specific techniques, such as optical coherence tomography (Donnelly et al., 2010; Coulman et al., 2011; Lutton et al., 2015b), that are not widely available. The field of mathematical modelling offers a promising avenue in this regard by allowing us to apply established theories for cost-effective and time-efficient advancements (Yadav et al., 2020; Sliwoski et al., 2013), e.g., they can predict MN material behaviour under various conditions.

When modelling the insertion of MNs into human tissue, understanding how the materials respond to insertion forces is crucial. Mechanical modelling can play a vital role in optimising the design and comprehending the impact of the material properties on MN performance (Liu et al., 2023). The integration of computational analysis, particularly through finite element analysis (FEA), enhances the safety and efficiency of MN-based drug delivery systems. FEA allows one to meticulously adjust the geometry, size, and material properties of MNs, ensuring optimal penetration with minimal discomfort and a reduced risk of breaking (Goel and Nyman, 2016; Chen et al., 2012). This strategic use of simulations facilitates a detailed analysis of MN interactions with skin layers, enabling precise adjustments to needle sharpness and length to specifically target tissues or improve drug delivery. Additionally, advanced simulation tools allow for the customisation of drug release profiles and enable predictions of MN behaviour

---

* Corresponding author.
E-mail address: d.b.das@lboro.ac.uk (D.B. Das).

https://doi.org/10.1016/j.ijpharm.2024.124620
Received 9 June 2024; Received in revised form 18 August 2024; Accepted 18 August 2024

under various stress conditions (Salahshoori et al., 2024). These tools are crucial for optimising insertion depths according to the needs of different therapeutic agents. For example, it has been defined that drugs with high water solubility can diffuse from the baseplate into the skin through the pores created by the array after the complete dissolution of the needle tip. On the other hand, other molecules, such as large proteins or highly hydrophobic drug suspensions, do not diffuse easily, and their administration is limited to the drug loaded into the needle tip (McCrudden et al., 2014, 2018). Therefore, the capacity to quickly and cost-effectively explore different design options through modelling is vital for enhancing drug delivery efficiency and ensuring patient safety, thereby, accelerating the development of new MN therapies (Avcil and Çelik, 2021).

In mechanical design, the application of numerical methods like FEA is vital for accurately predicting the physical attributes of the systems under various operational conditions (Jagota et al., 2013; Tanaka et al., 2000). Understanding and modelling the nonlinear mechanical behaviour of MNs during insertion is essential for their safe and effective use in medical applications (Wu et al., 2023b). This leads to more precise simulations, aids in design optimisation, and enhances our understanding of the effects of MN material properties. Incorporating nonlinear theories into the modelling of MNs bolsters design safety, develops precise models, and gains deeper insights into the materials' characteristics. This comprehensive approach not only ensures the safety and efficacy of MNs in medical applications but also supports ongoing innovation in MN technology, demonstrating the critical role of modelling in the evolution of medical devices (Marcé-Nogué, 2022).

Materials primarily exhibit two types of mechanical behaviour: linear and nonlinear elastic behaviours (Christian, 2017). Linear models, suitable for modest deformations where stress and strain maintain a proportional relationship, can be incorporated into the analysis by fundamental principles such as Hooke's Law, Young's Modulus, and Poisson's Ratio (Marcé-Nogué, 2022; Chabanas et al., 2006). For scenarios involving substantial deformations, nonlinear models, including the Power Law and Ramberg–Osgood, become crucial (Christian, 2017; Kim, 2015; Giardina and Wei, 2020). Incorporating these nonlinear models enhances the FEA method's ability to represent the complexities of material behaviour more accurately, particularly observed in MN. This improvement significantly broadens the FEA's versatility and its alignment with real-world applications, enabling it to simulate a broader spectrum of mechanical behaviours with higher fidelity.

Conversely, nonlinear hyperelastic models are crucial for representing the MN materials that undergo extensive deformations and exhibit nonlinear stress–strain behaviours. Hyperelasticity offers a fundamental framework for describing such behaviour, especially under finite-strain conditions. Consequently, stress–strain relationships, such as those given by neo-Hookean, Mooney–Rivlin, Ogden, and Yeoh, are vital for understanding pronounced material nonlinearities. They are enhanced by including additional parameters, broadening their applications to fields such as rubber technology and biomechanics (Khaniki et al., 2022; Trotta and Ní Annaidh, 2019; Fung, 1993; Martins et al., 2006).

Each hyperelastic model presents specific benefits and constraints. Therefore, the selection depends on the precision required and the nature of the deformation. The neo-Hookean model, known for its simplicity and stability, is optimal for isotropic materials under large deformations (Melly et al., 2021) and is suitable for modelling rubber-like materials within small to moderate strain ranges (González, 2016). However, its performance may diminish under very large strains or in complex scenarios (Kim et al., 2012). The Mooney–Rivlin model expands on the Neo-Hookean by better handling complex behaviours with additional parameters (Selvadurai, 2006). This paper aims to explore and analyse the nonlinear mechanical properties of both MN materials and skin, as well as the insertion behaviour of MNs into the skin, employing FEA simulations to achieve these objectives, validated with experimental procedures. The RO model (Gadamchetty et al., 2016) is used to study the chosen MN materials, as discussed in the methods and material section in detail. It is shown that the developed FEA model is effective in understanding how stress and strain interact in different MN materials. Additionally, the neo-Hookean model is utilised to study the specific mechanical behaviour of skin, which has demonstrated remarkable accuracy in describing skin's complex and nonlinear deformation as a soft biological tissue (Pissarenko, 2019). This investigation aims to provide valuable insights into the mechanical behaviour of materials and skin, with potential applications in biomechanics, medical devices, and tissue engineering. In real-world applications, an FE analyst often does not have access to the entire stress–strain curve of a material. Additionally, conducting immediate mechanical testing to obtain this information is not always feasible or practical. Therefore, we may need to work with limited or incomplete data when performing FEA. In our study, we utilised specific modelling techniques and detailed experimental data to mitigate the effects of limited or incomplete data. This included applying the RO and Neo-Hookean equations to model the nonlinear behaviours of MN materials and skin, respectively. Moreover, the transition of MN materials from powders to films is critical, as they acquire mechanical properties post-casting that are pivotal for effective MN function. Understanding these properties, influenced by polymer concentration, molecular weight, and polymer interactions within the casting gels, is essential for optimising MN design for safety and efficacy. We supplemented our computer simulations with measurements partly derived from experimental data and partly from mathematical calculations, such as Young's modulus, Poisson's ratio, reference stress, reference strain, and strain hardening. The paper's structure is carefully organised to comprehensively present the modelling, experimental investigation, and simulation analysis of MN interactions with skin. It is divided into several key sections, each designed to address specific aspects of our comprehensive study: introducing our foundational mathematical models, detailing the fabrication process, and providing deeper investigative insights into MNs' interactive behaviours. This structured approach thoroughly examines the critical elements influencing MN performance.

2. Governing equations

2.1. Ramberg–Osgood model for microneedles

The Ramberg–Osgood equation (R and Osgood, 1943; Gadamchetty et al., 2016) provides a simplified model to describe the stress–strain relationship for MN materials. In the case of uniaxial extension, the stress–strain relationship is defined by the following expression:

$$\epsilon = \frac{\sigma}{E} + \epsilon_{ref}(\frac{\sigma}{\sigma_{ref}})^{n} \tag{1}$$

where ϵ is strain, σ is stress, E is Young's modulus, and ϵ_{ref} is the strain at a reference stress σ_{ref}. The parameter n is the stress exponent. The parameter ϵ_{ref} is commonly chosen as 0.002, corresponding to the stress at 0.2% strain (denoted as $\sigma_{0.2}$ in literature) (Özkaya et al., 2017). This equation represents that the total strain is the sum of linear and nonlinear strains.

In this work, we apply the RO equation to depict how the MN materials undergo deformation and compression when subjected to external forces. This aspect is crucial for MNs, as the manner in which they deform and navigate through the dermal layers significantly influences their efficacy in therapeutic agent delivery. It is essential that the MNs penetrate the epidermis effectively with minimal resistance without inducing dermal damage. A deeper insight into these deformation behaviours allows for the optimisation of MNs to cater to diverse healthcare requirements, thereby enhancing the precision and patient comfort of treatment modalities.

2.1.1. Stress–strain relationship to extract the required parameters for RO model

Studying the nonlinear behaviour of PVP (Polyvinylpyrrolidone) and PVA (Polyvinyl Alcohol) materials used in MNs enables us to understand their mechanical properties and deformation characteristics, which are crucial for designing and applying MNs effectively. External forces induce movement and deformation in objects, with the latter occurring if motion is restricted. Deformation entails relative displacement within the object (MN in this case) and, is influenced by factors such as the magnitude and duration of the force, material properties, and geometry. It is known that the materials can exhibit diverse responses to different loading configurations (Özkaya et al., 2017). Therefore, controlled experiments are conducted to ascertain the mechanical properties of materials, e.g. the behaviour of materials under tensile loading can be examined through a uniaxial or simple tension test (Senthil Murugan and Jegan, 2017). Stress is the internal resistance or force a material experience when subjected to external forces, measured as force per unit area (σ). The study of these materials is essential for predicting how MNs will perform when inserted into the skin, including their ability to withstand the forces of insertion without breaking and their effectiveness in delivering therapeutic agents.

$$\sigma = \frac{E}{\epsilon} \tag{2}$$

Where σ denotes stress, E symbolises the elastic modulus (also known as Young's modulus), and ϵ signifies strain. Stress elucidates the force distribution within a material and is quantified in units such as Newtons per square metre ($\mathrm{N/m^2}$) or Pascals (Pa). Conversely, strain delineates the material's deformation or elongation when subjected to external forces, reflecting the proportional alteration in its dimensions relative to its original state. Represented by ϵ, strain is generally dimensionless or articulated as a percentage, calculated by the ratio of the change in length of the test specimen to its initial length.

$$\epsilon = \frac{L - L_0}{L_0} \tag{3}$$

L represents the current length of the material, and L_0 denotes the original length. This paper discusses the importance of stress and true strain in understanding material behaviour during plastic deformation, as they consider changes in cross-sectional area and a specimen's length during a tensile test. True stress is calculated by dividing the applied load by the specimen's instantaneous cross-sectional area, while true strain is determined using the natural logarithm of the ratio of the specimen's instantaneous length to its original length (Faridmehr et al., 2014; Anon., 2013). These measures provide a more accurate representation of a material's stress and strain, particularly in cases of significant plastic deformation (Faridmehr et al., 2014; Anon., 2013).

$$\sigma_{true} = \frac{\sigma_E}{1 - \epsilon_p} = \sigma(1 + \epsilon) \tag{4}$$

$$\epsilon_{true} = \ln(\frac{L}{L_0}) = In(1 + \epsilon) \tag{5}$$

Where σ_{true} denotes the true stress, and ϵ_{p} signifies the plastic strain Gadamchetty et al. (2016). To determine the reference stress (σ_{ref}), one identifies the point on the stress–strain curve where the strain equals 0.2%. The stress value corresponding to this strain level is designated as the reference stress (Özkaya et al., 2017). Similarly, to compute the reference strain (ϵ_{ref}), the point on the stress–strain curve where the stress matches the yield stress, or σ_{ref}, is located. The strain value at this specific stress point is then recognised as ϵ_{ref}.

The strain value at this specific stress point is then recognised as ϵ_{ref}. In the strain hardening exponent calculation, the logarithm of the reference strain and the corresponding reference stress values are utilised (Gubeljak, 2008; Total Material, 2023). This logarithmic transformation aids in analysing the relationship between stress and strain differently. Subsequently, the log of the actual stress is plotted against the true strain for the remaining data points on a graph. Linear regression techniques are then applied to determine the slope of the resulting log–log curve, representing the strain hardening exponent, which measures the material's ability to increase its resistance to deformation as strain accumulates (Total Material, 2023).

2.1.2. Neo-Hookean model for skin

As previously mentioned, the Neo-Hookean model is relatively simple and appropriate for isotropic materials with finite deformations, making it suitable for specific soft tissues. However, more complex nonlinear behaviour may need to be captured accurately (Kim et al., 2012). The Neo-Hookean model is implemented in the developed framework using the built-in material model named "Neo-Hookean". This model in COMSOL is formulated as:

$$W = \frac{\mu}{2}(\lambda_1^2 + \lambda_2^2 + \lambda_3^2 - 3) - \mu \ln(J) + \frac{\lambda}{2}(In(J))^2 \tag{6}$$

where W is the strain energy density function, μ is the shear modulus of the material, λ_1, λ_2, and λ_3 are the principal stretches. The J is the determinant of the deformation gradient.

The two material parameters needed for the Neo-Hookean model are the Lamé parameters, namely λ (stiffness coefficient) and μ (shear modulus) (Vaucorbeil et al., 2020). These parameters are related to Young's modulus (E) and Poisson's ratio (ν). The subsequent equations are utilised to compute the necessary parameters for the nonlinear model of skin:

$$\lambda = \frac{E \cdot \nu}{(1 + \nu) \cdot (1 - 2 \cdot \nu)} \tag{7}$$

$$\mu = \frac{E}{2 \cdot (1 + \nu)} \tag{8}$$

where E represents Young's modulus, and ν denotes Poisson's ratio. The calculated parameters are instrumental in defining the Neo-Hookean material model.

2.2. Experimental method and materials

This section presents a comprehensive overview of the experimental methodology and MN materials employed in the fabrication of MNs and other details utilised to analyse their insertion behaviour.

2.2.1. Microneedle manufacturing characterisation and insertion

To prepare MN arrays, a mixture of 20% w/w polyvinylpyrrolidone (PVP) (MW 58 kDa, Ashland Kidderminster, UK) and 20% w/w polyvinyl alcohol (PVA) (MW 10kDa, Sigma-Aldrich, Dorset, UK) in deionised water was moulded using laser-engineered silicone micromould templates, following established methods (Tekko et al., 2020; Larrañeta et al., 2014b). In brief, the formulations were placed inside the moulds and centrifuged at 3500 RPM for 10 min to fill the moulds. Subsequently, samples were allowed to dry inside the moulds for at least 28 h. After drying, the MN arrays were removed, and the sidewalls were trimmed with scissors. The MN arrays were further dried at 37 °C overnight. The moulds used for this study contained an array of 11 × 11 conical needles (Fig. 1) with a base width and interspacing of 300 μm and a needle height of 600 μm (Fig. 2).

The MN height was measured using a Leica EZ4 D digital microscope (Leica, Wetzlar, Germany). Additionally, MN insertion was evaluated using excised neonatal porcine skin which is considered a good model for human skin (Meyer, 1996). Neonatal porcine skin was excised from stillborn piglets and stored at −20 °C until used as described previously (Larrañeta et al., 2014a). Subsequently, it was defrosted before performing the experiment and carefully shaved before performing the insertion experiments. A TA.XTPlus Texture Analyzer (Stable Micro Systems, Surrey, UK) was used to apply a force of 32N for 30 s at a speed of 0.5 mm/s (Lutton et al., 2015a; Peng et al., 2021; Cárcamo-Martínez et al., 2021; Angkawinitwong et al., 2020). Subsequently, the inserted MN arrays were immediately examined using an

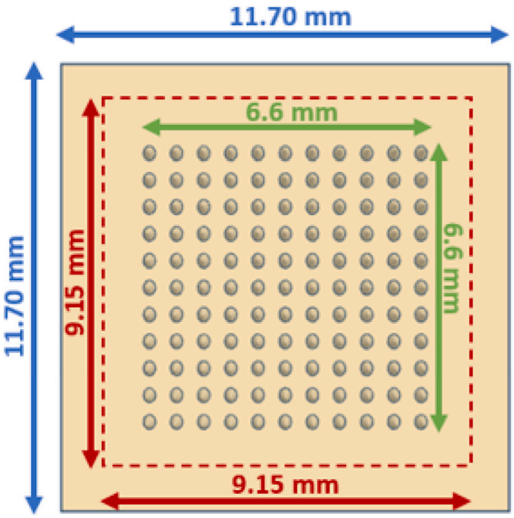

Fig. 1. Illustration depicting MN patches with dimensions of 11 × 70 mm .

EX1301 Optical Coherence Tomography Microscope (Michelson Diagnostics Ltd., Kent, UK). The obtained 2D images were analysed using ImageJ@ software (National Institutes of Health, Bethesda, USA). The image files were scaled, with 1.0 pixel representing 4.2 μm, enabling precise measurements of MN penetration depth and pore width. Two different arrays were inserted, and the average insertion depth was measured. For this purpose, at least 20 measurements were performed across both arrays.

2.3. Simulation details

COMputational SOLutions (COMSOL) software is a powerful and versatile platform that utilises the FE methods (COMSOL Multiphysics® v. 6.1). Simulations were conducted using the Structural Mechanics Module of COMSOL (Multiphysics, version 6.1) to model a patch of 8 × 8 of cone-shaped. COMSOL provides the flexibility to incorporate the RO equation as a constitutive model to describe the nonlinear behaviour of materials.

In order to reduce simulation times, a downscaled patch of 8 × 8 was utilised, as opposed to the original configuration of 11 × 11 MNs. The MNs had a height of 518 μm, and its base diameter of 300 μm, with a tip diameter of 8 μm. The interval space (pitch) between needles is 300 μm. The 3D geometry of the MNs was generated using a geometrical tool, and a nonlinear elastic material model was applied to represent the MNs. In contrast, hyperelastic material properties were used to model the skin. The material properties were obtained from the partially calculated and computed parameters in Table 1 for simulations. Young's modulus values were determined through tensile tests conducted in the experimental procedure, while the remaining parameters were calculated using our custom-developed MATLAB (MathWorks. (2019). MATLAB, version R2019a) scripts. In the implementation of the Neo-Hookean model, λ and μ can be articulated as functions of E and ν. The units for λ and μ are customarily akin to those of Young's Modulus, expressed as force per unit area (N/m^2 or Pascals, Pa), adjusted by a dimensionless ratio.

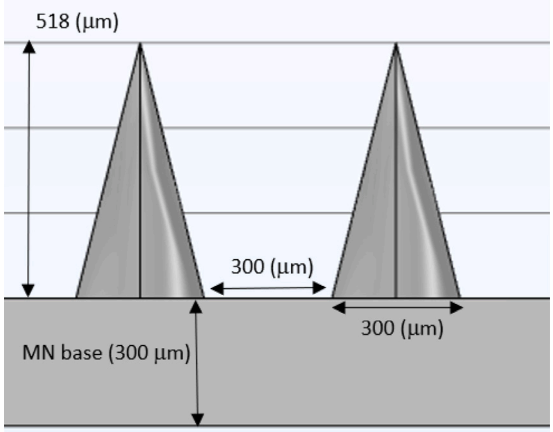

Fig. 2. Schematic representation of MN geometry, and shape.

Table 1
Mechanical and physical properties of the PVP+PVA dissolving polymer.

Parameter	Calc.	Computed
Density (kg/m^3)	1135	1135
Young's Modulus (GPa)	0.77	0.77
Tensile Strength (MPa)	8.36	8.47
Strain Hardening (n)	0.32	0.33
Reference Stress (MPa)	6.9	6.8
Reference strain (%)	0.6	0.34
Stress exponent (%)	0.6	0.75

Additionally, Fig. 3 illustrates the structural arrangement of the skin as generated by the COMSOL simulation. Notably, the skin's textural roughness was introduced using the parametric surface module within COMSOL, thus enhancing the realism of the model and its ability to capture complex skin features. In our model, the skin is represented by three distinct layers, each with specific biomechanical attributes, the stratum corneum (SC), the outermost layer at 20 μm thick, has a density of 1300 kg/m^3 and a high Young's Modulus of 0.2E5 Pa, denoting its rigidity. The Epidermis follows with a thickness of 150 μm, a slightly lower density of 1200 kg/m^3, and a Young's Modulus of 0.1E5 Pa, reflecting a balance of protection and pliability. The dermis, the thickest layer at 2000 μm, has the same density as the Epidermis, and its mechanical properties are similar, enabling the skin to maintain structural integrity and flexibility. These layered parameters are critical for simulating realistic skin behaviour under mechanical stresses in various biomedical scenarios.

In this section, we present the development of a multilayer model of human skin employing the FE method, carefully designed to mirror the complex mechanical behaviour of the skin across its various layers, from the SC down to the dermis. A notable advancement in our model is the incorporation of surface roughness and topology into the SC layer. This critical feature emulates the inherent roughness observed on the outermost layer of real human skin. While enhancing the model's fidelity to actual skin properties, this addition introduces new challenges in simulating MN penetration. This innovative aspect of our model aims to provide deeper insights into the interaction between MNs and the skin's outermost barrier, potentially influencing the design and optimisation of MN-based drug delivery systems.

Table 2 lists the mechanical specifications of each layer. The skin structure comprises three primary layers: the SC, epidermis, and dermis. The SC, the outermost layer, acts as the skin's protective barrier, with a thickness of approximately 20 μm (Mohammed et al., 2012; Czekalla et al., 2019). Beneath it lies the epidermis, a vital layer for maintaining the skin's integrity, which measures around 150 μm in our simulation (Pissarenko and Meyers, 2020). Deeper still is the dermis, a thicker layer with a thickness of 2000 μm. To reduce simulation time, we have set the dermis thickness to 800 μm whilst preserving its mechanical properties. All the dimensions have been derived from Wei et al. (2017). Lamé's first and second parameters were computed by utilising the pertinent published data and were subsequently added to Table 2.

By incorporating these dimensions and mechanical property values in our simulation, we aim to gain insights into the skin's mechanical behaviour and advance our understanding of its response upon

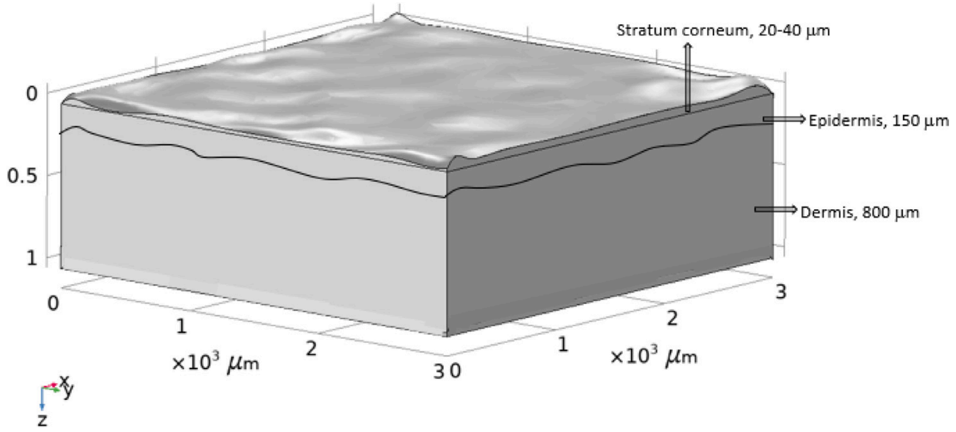

Fig. 3. The skin's layered structure from top to bottom, consisting of the stratum corneum, epidermis, and dermis.

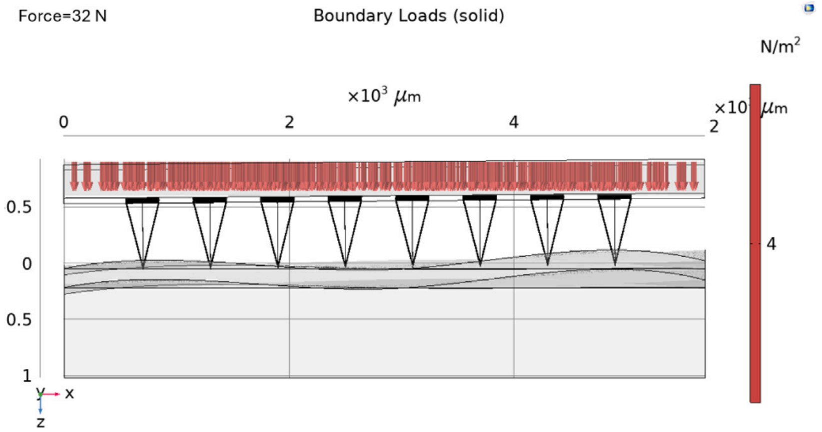

Fig. 4. Illustration of boundary load on the base of MN's patch in COMSOL.

Table 2
Mechanical specifications of skin layers.

Parameters	Skin layers		
	Stratum corneum	Epidermis	Dermis
Density (Kg/m^3)	1300	1200	1200
Poisson's ratio	0.49	0.42	0.42
Young's Modulus Pa	$0.2E^5$	$0.1E^7$	$0.1E^9$
Thickness (μm)	20	150	2000
Stiffness coefficient (μ) Pa	328 859	1848591.5	184859154.1
Shear modulus (λ) Pa	6711.4	352 112.7	35211267.7

MN insertion. A hyperelastic approach was employed to simulate the nonlinear behaviour of skin, utilising the neo-Hookean constitutive equation. This choice of model enabled the accurate representation of the skin's response under varying deformation conditions.

This mathematical modelling facilitates a comprehensive analysis of stress distribution and penetration depth concerning MNs. This analysis included the simulation of Von-Mises stress as well as the deformation of both MNs and the skin, all under stationary conditions. A boundary load was applied to the top of the MN patch, as shown in Fig. 4, while a fixed constraint was placed on the surrounding skin. This setup allowed the MNs to move exclusively along the axial direction, penetrating the skin. The study covered a range of forces, progressively increasing from 5 to 15 N. The outcomes of these simulations provided a clear visualisation of stress distribution patterns and penetration depths, thus offering insights into the intricate mechanical interactions between MNs and the skin under various force magnitudes.

3. Results and discussion

Developing computer models to understand and predict MN performance could accelerate the development of new MN products. Understanding the insertion of these devices is especially important because the drug administration of one of the most used types of MNs, dissolving MN arrays, relies on the dissolution of the inserted needle tip to release the drug cargo. Therefore, deeper insertion depths will contribute to a higher amount of drug released. However, it is important to mention that depending on the nature of the drug molecule insertion depth is not the only key parameter controlling drug delivery. It has been reported previously that drug loaded in non-inserted sections of the MN array such as the baseplate can diffuse inside the skin through the created pores after MN dissolution. This has been reported for hydrophilic drug molecules. However, for hydrophobic drugs, drug micro/nano suspensions, or large molecules, diffusion into the skin through the created pores can be difficult (Donnelly et al., 2010; Coulman et al., 2011; Lutton et al., 2015b). Therefore, understanding insertion could inform the formulation of MN arrays to decide on parameters such as drug loading and whether the drug should be located primarily on the needle tips. Additionally, developing mathematical models will save time and materials by reducing the number of formulations that need to be developed and tested. It is also important to note that evaluating MN insertion is not a simple task (Lutton et al., 2015b). So far, the only reliable tool to evaluate MN insertion is optical coherence tomography, which is not widely available. Thus, in silico models to predict MN insertion are highly valuable for informing and rationalising MN design, while reducing the number of experiments and minimising material and drug wastage (Yadav et al., 2022). In this

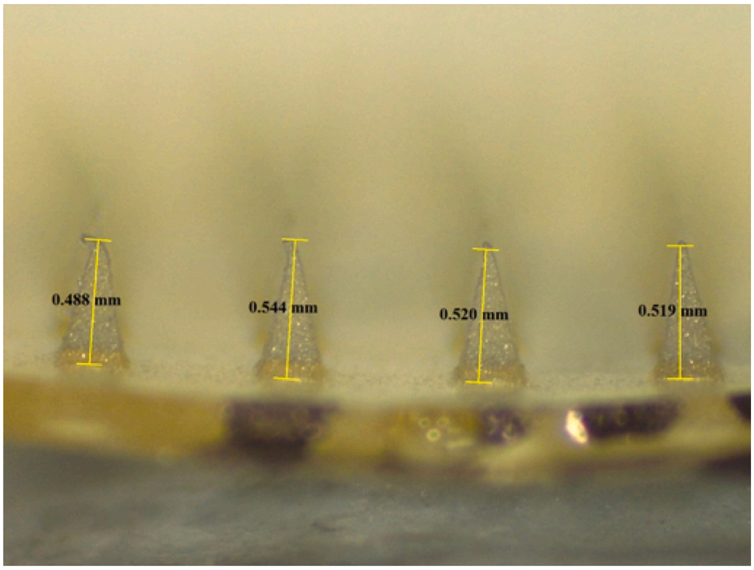

Fig. 5. Representative digital image of MN prepared in this study.

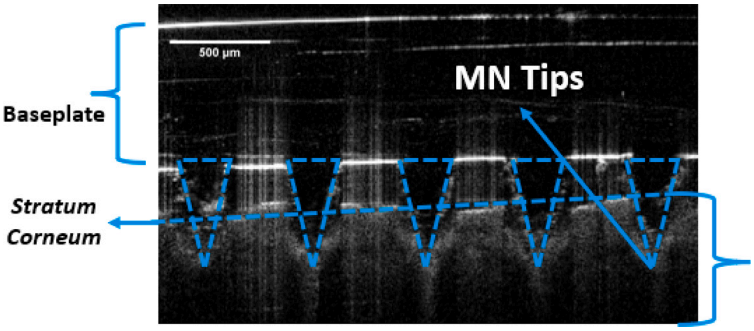

Fig. 6. Optical coherence tomography (OCT) image with graphical lines illustrating borders between MNs and stratum corneum.

work, we have focused on a dissolving MN type based on a combination of PVP and PVA, as this particular dissolving MN formulation has proven to be highly relevant and has been used extensively, even in vivo animal models (Anjani et al., 2023; David et al., 2023; Anjani et al., 2024; Wu et al., 2023a; Xiao et al., 2024; Nasiri et al., 2022b).

3.1. Experimental findings

A detailed examination of the MN patch revealed that the needles were organised in an array of 121, configured into an 11 × 11 grid, with each needle exhibiting a conical shape. The MN arrays, produced using micromoulds, were examined using optical microscopy. The observed needle height was found to be less than the anticipated 600 μm. Representative images of the MN arrays manufactured in this study are displayed in Fig. 5. The average height of the needles was recorded at 518 μm. This reduction in size, often referred to as shrinkage, is a well-documented occurrence associated with silicone moulds (Lutton et al., 2015a).

3.1.1. OCT images of fabricated microneedles

Subsequently, MN arrays were inserted into excised neonatal porcine skin. Fig. 2 displays representative Optical Coherence Tomography (OCT) images showcasing the penetration of MNs into the porcine skin. The average depth of insertion was measured to be 283 ± 26 μm. Considering that MN measured 518 μm in length before penetration the insertion depth is higher than 50% of the initial needle length. These findings are consistent with the insertion depths of MN arrays reported in prior studies (Larrañeta et al., 2014b). This depth of penetration conclusively demonstrates the MN's full insertion beyond the SC and into the epidermis.

3.2. Simulations

3.2.1. Penetration depth

In the investigation of MNs penetration through the skin layers, two cross-sectional views (Figs. 7 and 8) clearly show the journey of the MNs through the intricate layers of the skin: the SC, epidermis, and dermis. Fig. 7 focuses on the overall penetration depth and the interaction of MNs with the skin layers, with the skin layers being transparent to show both initial and final positions. Fig. 8 emphasises the cross-sectional view of a smaller part of the MN patch, showcasing the non-uniform penetration due to skin roughness and the visibility of MN tips in the dermis. Both figures use the same scale bar to indicate displacement in micrometres, ensuring consistency and aiding in comparing the figures. The x-y-z annotation indicates spatial orientation, with x-axis as the horizontal direction, y-axis as the vertical direction, and z-axis as the depth.

From Fig. 9, it was observed that almost 100% of MNs successfully penetrated to a depth of about 250 μm, reaching the outermost layer of the skin known as the SC, and ultimately the epidermis. It appears that more than half of these MNs successfully achieved a penetration depth of about 380 μm into the third layer. These results were in good agreement with the data collected from the experimental part of this study. This observation also highlights the complex nature of the skin's composition and its varying responses to MNs penetration.

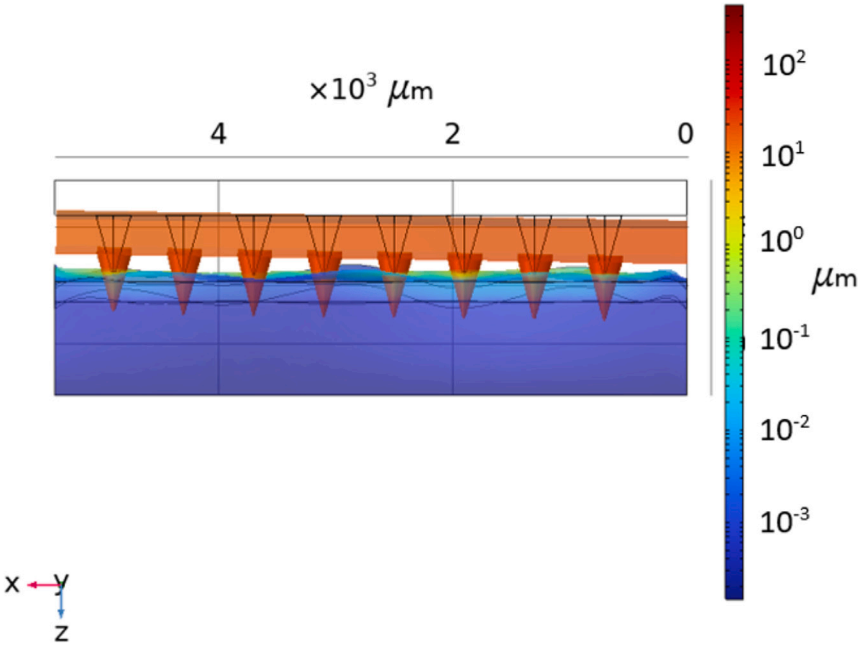

Fig. 7. Visualisation of MNs penetration into skin layers: Colour bar represents penetration depth in micrometres at 32 N force at μm magnitude. The skin layers are transparent to show both the initial position and the end position where the MNs penetrated to the dermis. The x-y-z annotation indicates spatial orientation.

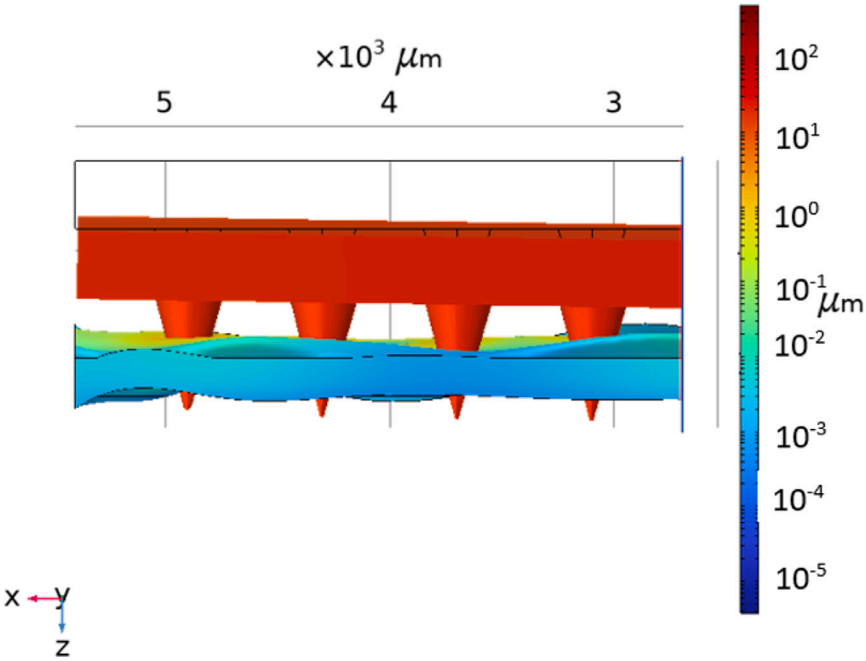

Fig. 8. Cross sectional view of MNs penetrating the stratum corneum and epidermis at 32 N force at μm magnitude. This image shows a small part of the MN patch, highlighting the non-uniform penetration due to skin roughness, where the tip of each MN is visible in the dermis. The scale bar represents displacement in micrometres. The x-y-z annotation provides spatial orientation.

These findings are consistent with the results reported by Yan et al. (2021) which provide a solid benchmark for our study. Specifically, the actual penetration depths reported by Yan et al. for various composite materials, such as CMC:PVP and CMC:PVA, show penetration depths ranging from 262 μm to 469 μm depending on MN composition. The MNs described in this study made mainly of PVA or PVP showed insertion depths (ca. 300 μm) like the ones reported here. The consistency between these two studies underscores the reliability of our experimental approach and supports the effectiveness of MNs in traversing the targeted skin layers for therapeutic purposes.

Further supporting our results is the study conducted by Muhammad Iqbal Nasiri et al. (2022a) which elucidates the robustness and effective penetration capabilities of dissolving MNs. In their research, MN arrays prepared using 40% PVA and 60% PVP demonstrated strong skin insertion, achieving depths of approximately 400–460 μm in neonatal porcine skin and penetrating up to 500 μm into the 4th layer of Parafilm, which mimics human skin. These penetration depths were attained without significant structural compromise, as evidenced by less than a 10% reduction in MN height under a compression force of 32 N. It is important to mention that the needles used in this study were

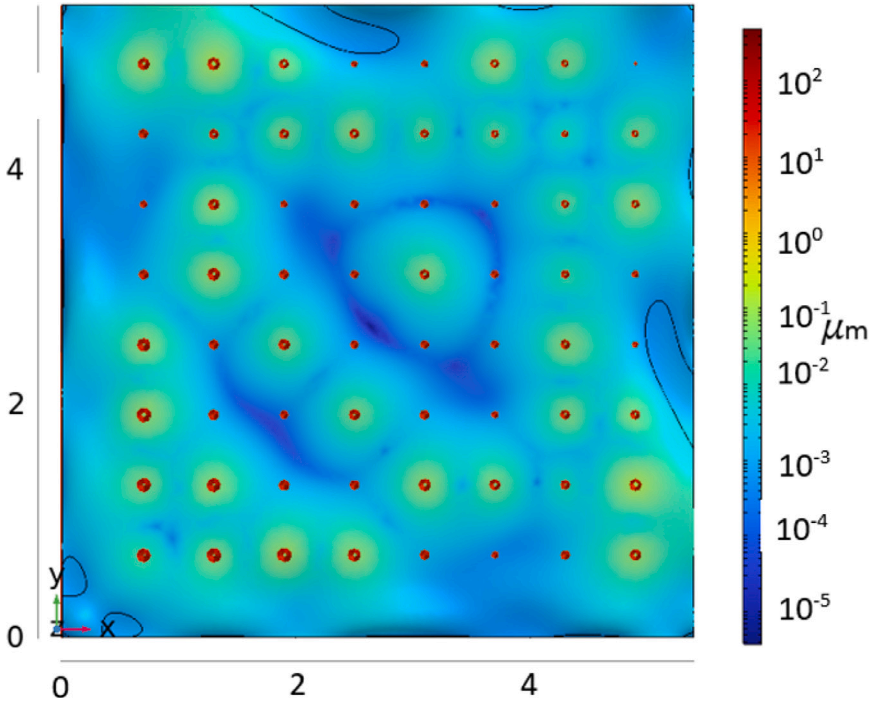

Fig. 9. View of MNs penetrating the third layer (dermis) from a Z–X perspective at μm magnitude. The x-y-z annotation indicates spatial orientation.

longer than the ones modelled here. Therefore, these results suggest that the model developed here could be used to predict successfully MN insertion.

Fig. 7 additionally reveals uneven MN penetration through the skin layers, with the MN patch marginally inclined to one side. This variation might be attributed to the incorporation of skin roughness in the simulation, leading to disparities in SC thickness across the skin's surface. Areas exhibiting higher roughness and a thinner SC tend to allow for easier MN penetration, potentially resulting in uneven penetration depths. These insights highlight the necessity of considering skin heterogeneity in MN designs to ensure uniform and precise penetration for diverse applications.

Moreover, Fig. 7 showcases substantial displacement within the MNs, as indicated by the colour bar in the figure. MNs are depicted in a reddish hue, denoting significant displacement, while the skin layers show minimal displacement, represented by the blue colour at the lower end of the colour spectrum.

In terms of MN penetration, minimising skin deformation is considered advantageous, correlating with more homogeneous needle penetration (Cai et al., 2022). This advantage is largely due to the slight resistance between the needle and human skin (Jiang et al., 2016). When MNs cause less lateral movement of the skin, it results in more consistent delivery and minimises the risk of unintended tissue damage, promoting faster healing and recovery (Makvandi et al., 2021b). Ultimately, reduced skin displacement enhances the overall acceptance and safety of MN-based treatments for various applications, including drug delivery and diagnostics.

The data obtained from experiments using OCT were corroborated by comparison with simulations Fig. 10. These images exhibit a significant agreement with the OCT findings, demonstrating that approximately 300 μm to 380 μm of the MNs' total length was successfully inserted into the skin. An observation from the accompanying image is the slight tilt of the MNs in one direction, as depicted in Fig. 6. The dissolving MNs, composed of PVP/PVA and devoid of any payload, achieved a depth of about 300 μm when subjected to a force of 32 N, with the SC still visible. This result conclusively confirms the MNs' sufficient mechanical robustness to penetrate porcine skin effectively.

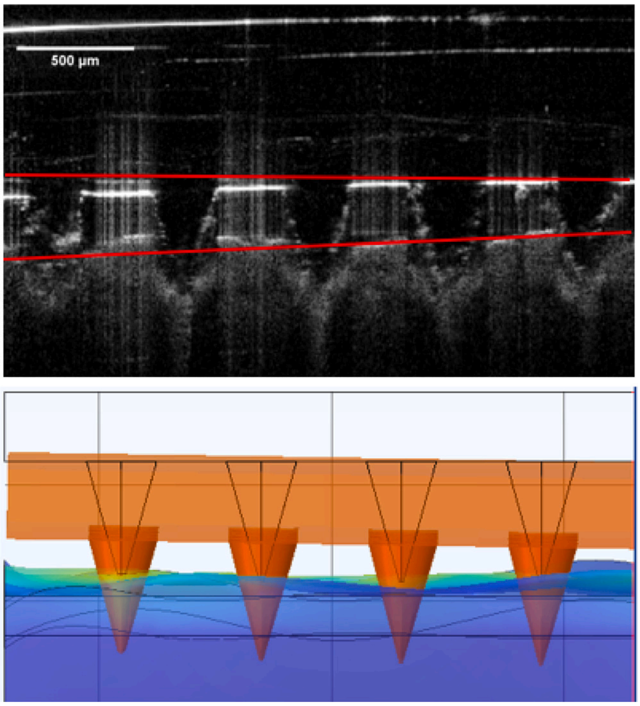

Fig. 10. Optical coherence tomography (OCT) image showing MNs penetrating the skin compared with the image from the simulation.

3.2.2. *Stress distribution*

Building upon the data collected through our experimental tests and the insights from our simulation studies, we embarked on an in-depth investigation. The goal was to delve deeper into the complex dynamics of stress distribution within both the MNs and the skin. In this section, we present the data collected using the same setup as in our simulation studies.

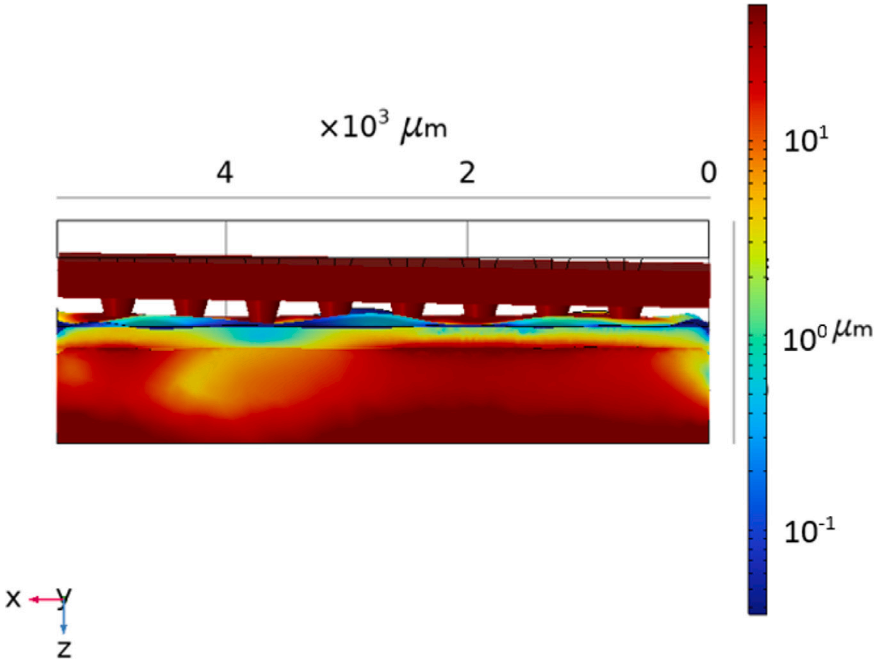

Fig. 11. Cross-sectional view of MNs depicting stress distribution in skin layers and MNs at 32 N force. The scale bar represents von Mises stress in N/m^2. The x-y-z annotation indicates spatial orientation.

Fig. 11 offers a comprehensive view of the stress distribution pattern within the three skin layers from a cross-sectional yx perspective in the simulation environment. The areas of the skin where MNs could successfully penetrate through the layers exhibit lower stress levels within the SC. This is likely due to the MNs effectively overcoming the resistance posed by the SC, encountering less stress as they penetrate deeper into the skin. The colour map, showing cooler colours (such as blue or green), indicates lower stress levels, suggesting that these regions experience relatively smoother and less obstructive penetration. Notably, some needle tips are visibly protruding from the dermis layer, coloured red. Conversely, areas where MNs could not pass through show higher stress levels, as indicated by warmer colours (yellow and red) on the colour map. In these regions, the MNs are facing more resistance and are likely unable to penetrate the skin layers effectively. The higher stress suggests that the MNs are experiencing greater force, which may cause potential deformation as they attempt to breach the SC.

In recent years, FEA method has gained traction for testing and validating the mechanical properties of polymer MNs, complementing experimental research. Integrating these insights with the findings of Chui-Yu Chiu et al. (2012), who found that conical MNs, especially those with smaller base diameters (100 μm), exhibited much higher stress than those with a larger base diameter (200 μm), emphasises the impact of base size on mechanical resistance. Our study utilised conical MNs with a 300 μm base diameter and identified relatively lower stress levels across the SC, underscoring how increasing the base size can help MNs penetrate more efficiently with reduced stress. Together, these results reinforce the importance of shape and base diameter in stress distribution and MN durability. In another study, Loizidou et al. (2015) conducted an FEA study to investigate the mechanical characteristics of sugar MNs, using buckling force and von Mises stress as indicators of potential needle failure. Their findings revealed a strong correlation between the material's Young's modulus, the critical flexion load at which MNs fail, and the penetration depth. This underscores the value of combining FEA with experimental studies to better predict the mechanical behaviour of different MN materials, ultimately supporting the development of more efficient and robust MN designs. Fig. 12 provides insights into the penetration dynamics and stress distribution of MNs within the epidermal layer at 32 N force. The horizontal axis (x-axis) represents the lateral position across the MN array, while Z-axis represents the depth of penetration into the skin layers. The colour gradient on the right side provides a scale for the stress levels, enhancing the comprehension of stress distribution patterns. The focus is on illustrating the interaction between the MNs and the upper layers of the skin, namely the stratum corneum and the epidermis. By focusing on a part of the MNs, the figure provides insight into the penetration process at a more granular level. It reveals the extent to which the MNs can penetrate the skin's upper layers and reach the dermis, which is crucial for their effectiveness in delivering substances or measuring parameters beneath the skin surface. Notably, in the second epidermal layer, heightened stress levels are observable, represented by an increased presence of blue and green regions on the colour map. This colour pattern signifies more significant stress concentrations in these areas. Within one corner, some MN tips are visible. The stress distribution within the MN patch appears notably elevated, evident by the dark red colour on the colour bar spectrum. The areas of dark red indicate regions of significant stress, not only at the tips of the MNs but also in the surrounding skin areas, highlighting the extent of mechanical influence exerted by this force level. Such uniform and elevated stress across the contact area suggests that the force of 32 N is more than sufficient to ensure the MN array's penetration. As mentioned earlier this force was measured to be the average force applied by human volunteers to insert MN arrays. Also, manual application by human volunteers has demonstrated to be safe as no adverse effects or pain was reported (Ripolin et al., 2017; Al-Kasasbeh et al., 2020).

Similar to our findings, Kong et al. (2011) developed a comprehensive multilayer skin model including the SC, dermis, and hypodermis to study the mechanical interaction during MN insertion. They employed finite element analysis to predict the complete insertion process, factoring in the mechanical properties of the skin and the MN geometry. Their results, which align with experimental data, underline the pivotal role of skin properties such as stiffness and failure stress in determining the necessary insertion force. Kong et al.'s study sheds light on how variations in MN geometry such as tip area impact the insertion force,

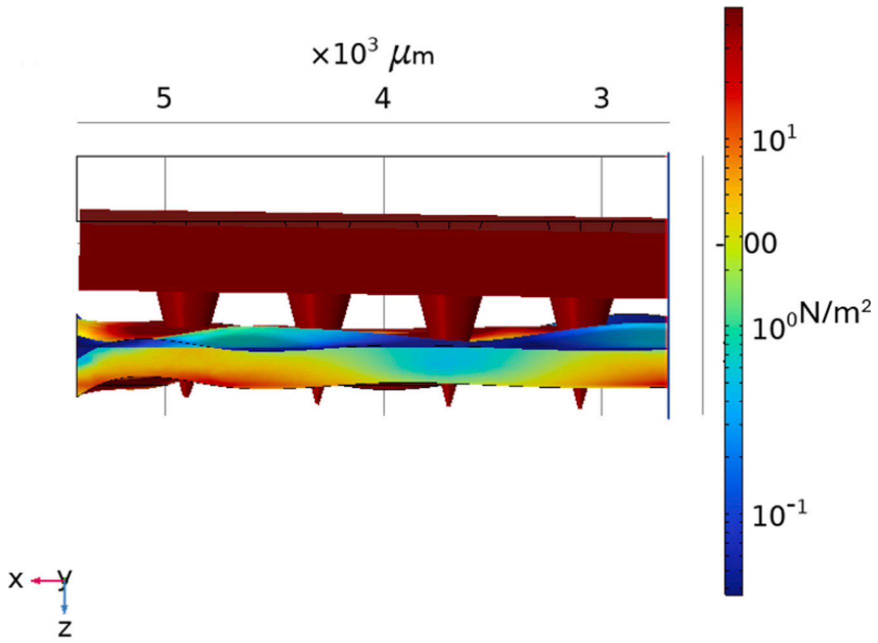

Fig. 12. A cross-sectional view of MNs illustrates the stress distribution within the epidermis under a force of 32 N. Only stratum corneum and epidermis are visible in this figure. The x-y-z annotation indicates spatial orientation.

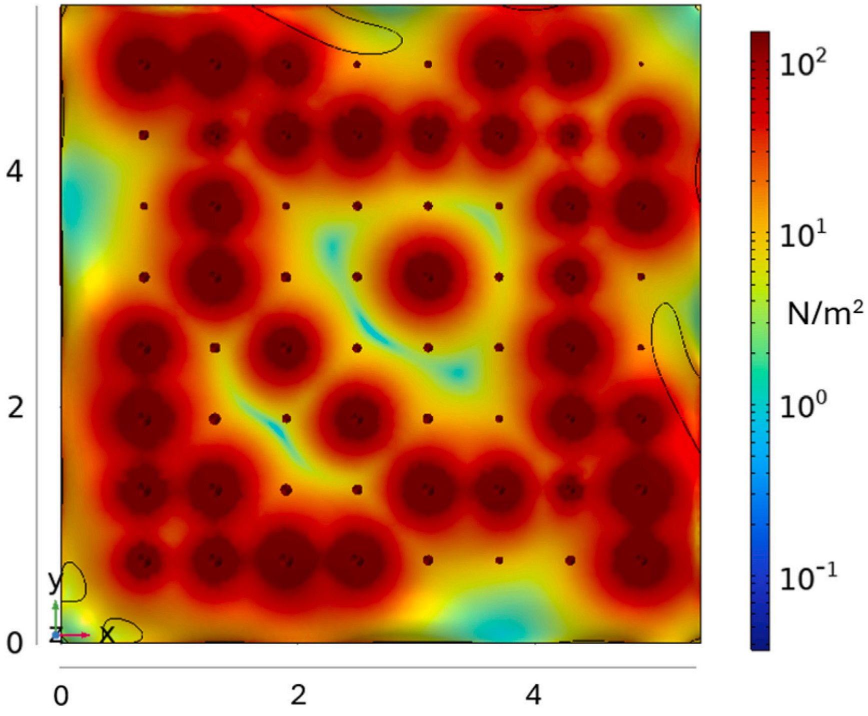

Fig. 13. The stress distribution within the second layer (epidermis), observed from a Z–X perspective. The scale bar represents von Mises stress in N/m^2.

a factor that our study aligns with in showing how force distribution varies with different MN configurations. Drawing parallels between these detailed analyses, our study expands on Kong et al.'s findings and enhances our understanding of how the mechanical properties of skin and MN design influence the efficiency of transdermal drug delivery systems. Such comparisons are essential for optimising MN designs to ensure minimal discomfort while providing effective penetration and drug delivery.

Fig. 13 illustrates a comprehensive view of stress distribution within the hypodermal layer from a Z–X perspective. Notably, a distinct concentration of stress surrounds the needle tips, visibly represented by the intense red colour on the colour bar spectrum. Some regions exhibit smoother surface characteristics, as indicated by shades of yellow and blue on the colour scale, resulting in lower stress levels. This can be primarily attributed to surface roughness, which significantly contributes to variations in stress levels. Elevated stress during MN skin penetration is undesirable as it can cause pain, tissue damage, and inconsistent drug delivery. Minimising stress ensures patient comfort, safety, and treatment effectiveness. Our findings support the importance of considering variations in skin properties, such as SC thickness and roughness, when designing MNs for various applications. Optimising MN design to effectively overcome resistance in non-penetrable areas while maintaining desirable stress levels in penetrable regions is a crucial challenge for consistent and reliable penetration (Makvandi et al., 2021b). However, it is important to mention that the insertion forces of similar MNs in human volunteers have not generated pain (Ripolin et al., 2017; Al-Kasasbeh et al., 2020). Therefore we can extrapolate that the stress values generated in this model will not result in pain/discomfort during insertion. However, the model described here can be used to monitor stress distribution for other geometries to minimise it. Therefore, the model developed here provides a valuable tool to design optimum MNs arrays and to reduce experimental iterations during MN development.

The detailed stress distribution pattern, as shown in the visual representation in Fig. 13, allows for pinpointing specific areas where the stress concentration significantly deviates from the surrounding regions. The darker red zones around the needle tips suggest areas of high mechanical interaction and potential focal points for localised tissue disruption or discomfort. These observations imply that the mechanical design of the needles, along with their insertion strategy, must be meticulously planned to distribute stress more uniformly across the contact surface, thereby reducing peak stress zones. Such adjustments could enhance the overall efficacy of transdermal applications by reducing the mechanical stress footprint, which is critical for both patient comfort and therapeutic outcomes. Our results emphasise the need for precise engineering and design considerations in the development of MN technologies to tailor stress distributions that align with the dermatological and therapeutic requirements.

4. Conclusions

This experimental study has provided significant insights into the efficacy of MNs with respect to their penetration depth and interaction with the skin. These findings are closely aligned with data from computational simulations performed in COMSOL, affirming the accuracy of the mechanical testing and mathematical calculations used for both PVP/PVA and skin. Such precision is critical as it informs future research by elucidating the interactions between MNs and dermal layers.

Advanced simulations have further deepened our understanding of stress distribution within the skin and MNs during insertion. These insights allow for the optimisation of MN designs prior to the development of prototypes. In this way, MN performance can be predicted prior to developing a formulation., This is critical to understand the performance of these devices as depending on the physicochemical nature of the drug cargo the insertion will predict the amount of drug administered. Moreover, the information obtained by the model developed here can be used to predict MN stability during insertion. The ability to finely adjust MN configurations based on precise simulation data underscores the potential of computational tools in advancing MN technology. Ultimately, the integration of experimental results and advanced simulation provides a robust foundation for developing MN systems that optimally balance patient comfort with therapeutic efficacy. This collaborative approach promises to drive further innovations in the field, advancing the development of MN technologies that meet clinical needs effectively.

CRediT authorship contribution statement

M. Soorani: Writing – review & editing, Writing – original draft, Methodology, Formal analysis, Data curation, Conceptualization. **Q.K. Anjani:** Writing – review & editing, Data curation. **E. Larrañeta:** Writing – review & editing, Supervision, Resources, Conceptualization. **R.F. Donnelly:** Writing – review & editing, Supervision, Funding acquisition, Conceptualization. **D.B. Das:** Writing – review & editing, Supervision, Project administration, Methodology, Investigation, Funding acquisition, Conceptualization.

Declaration of competing interest

The authors declare the following financial interests/personal relationships which may be considered as potential competing interests: DIGANTA BHUSAN DAS reports financial support was provided by Engineering and Physical Sciences Research Council. If there are other authors, they declare that they have no known competing financial interests or personal relationships that could have appeared to influence the work reported in this paper.

Data availability

Data will be made available on request.

Acknowledgements

We thank the Engineering and Physical Sciences Research Council (EPSRC) for supporting this work under grant EP/V047221/1, which has made this work possible. Special thanks go to our collaborators at Medical Biology Centre, Queen's University Belfast, whose contributions were invaluable to this project.

References

Al-Kasasbeh, R., Brady, A., Courtenay, A., Larrañeta, E., McCrudden, M., O'Kane, D., Liggett, S., Donnelly, R., 2020. Evaluation of the clinical impact of repeat application of hydrogel-forming microneedle array patches. Drug Deliv. Transl. Res. 10, http://dx.doi.org/10.1007/s13346-020-00727-2.

Aldawood, F.K., Andar, A., Desai, S., 2021. A comprehensive review of microneedles: Types, materials, processes, characterisations and applications. Polymers 13 (16), 2815. http://dx.doi.org/10.3390/polym13162815, PMID: 34451353; PMCID: PMC8400269.

Ang, U., Courtenay, A., Rodgers, A., Larrañeta, E., McCarthy, H., Brocchini, S., Donnelly, R., Williams, G., 2020. A novel transdermal protein delivery strategy via electrohydrodynamic coating of PLGA microparticles onto microneedles. ACS Appl. Mater. Interfaces http://dx.doi.org/10.1021/acsami.9b22425.

Angkawinitwong, U., Courtenay, A.J., Rodgers, A.M., Larrañeta, E., McCarthy, H.O., Brocchini, S., et al., 2020. A novel transdermal protein delivery strategy via electrohydrodynamic coating of PLGA microparticles onto microneedles. ACS Appl. Mater. Interfaces 12 (11), 12478–12488.

Anjani, Q.K., Nainggolan, A.D.C., Li, H., Miatmoko, A., Larrañeta, E., Donnelly, R.F., 2024. Parafilm® M and Strat-M® as skin simulants in vitro permeation of dissolving microarray patches loaded with proteins. Int. J. Pharm. 655, 124071. http://dx.doi.org/10.1016/j.ijpharm.2024.124071.

Anjani, Q.K., Pandya, A.K., Demartis, S., Domínguez-Robles, J., Moreno-Castellanos, N., Li, H., Gavini, E., Patravale, V.B., Donnelly, R.F., 2023. Liposome-loaded polymeric microneedles for enhanced skin deposition of rifampicin. Int. J. Pharm. 646, 123446. http://dx.doi.org/10.1016/j.ijpharm.2023.123446.

Anon., 2013. StandArd Test Methods for Tension Testing of Metallic Materials. Department of Defense. Editor. American Society for Testing and Materials (ASTM.

Avcil, M., Çelik, A., 2021. Microneedles in drug delivery: Progress and challenges. Micromachines 12 (11), 1321. http://dx.doi.org/10.3390/mi12111321, PMID: 34832733; PMCID: PMC8623547.

Cai, Y., Huang, S., Zhang, Z., Zhang, J., Zhu, X., Chen, X., Ding, X., 2022. Bioinspired rotation microneedles for accurate transdermal positioning and ultraminimal-invasive biomarker detection with mechanical robustness. Research 2022, 1–15. http://dx.doi.org/10.34133/2022/9869734.

Cárcamo-Martínez, Á., Mallon, B., Anjani, Q.K., Domínguez-Robles, J., Utomo, E., Vora, L.K., et al., 2021. Enhancing intradermal delivery of tofacitinib citrate: Comparison between powder-loaded hollow microneedle arrays and dissolving microneedle arrays. Int. J. Pharm. 593, 120152.

Chabanas, M., Payan, Y., Marecaux, C., Swider, P., Boutault, F., 2006. Comparison of linear and non-linear soft tissue models with post-operative CT scan in maxillofacial surgery. Lecture Notes in Comput. Sci. http://dx.doi.org/10.1007/978-3-540-25968-8_3.

Chang, H., Chew, S., Zheng, M., Lio, D., Wiraja, C., Mei, Y., Ning, X., Cui, M., Than, A., Shi, P., Wang, D., Pu, K., Chen, P., Liu, H., Xu, C., 2021. Cryomicroneedles for transdermal cell delivery. Nat. Biomed. Eng. 5, 1–11. http://dx.doi.org/10.1038/s41551-021-00720-1.

Chen, Shuhu, Li, Nannan, Chen, Jing, 2012. Finite element analysis of microneedle insertion into skin. IET Micro Nano Lett. 7, 1206–1209. http://dx.doi.org/10.1049/mnl.2012.0585.

Chiu, C., Kuo, H., Lin, Y., Lee, J.-L., Shen, Y.-K., Kang, S., 2012. Optimal design of microneedles inserts into skin by numerical simulation. Key Eng. Mater. 516, 624–628.

Christian, L., 2017. Linear and Non-Linear Mechanical Behaviour of Solid Materials. http://dx.doi.org/10.1007/978-3-319-55609-3.

COMSOL Multiphysics® v. 6.1, [Online]. Available: www.comsol.com. COMSOL AB, Stockholm, Sweden.

Coulman, S.A., Birchall, J.C., Alex, A., et al., 2011. In vivo, in situ imaging of microneedle insertion into the skin of human volunteers using optical coherence tomography. Pharm. Res. 28, 66–81. http://dx.doi.org/10.1007/s11095-010-0167-x.

Czekalla, C., Schoenborn, K.-H., Lademann, J., Meinke, M., 2019. Noninvasive determination of epidermal and stratum corneum thickness in vivo using two-photon microscopy and optical coherence tomography: Impact of body area, age, and gender. Skin Pharmacol. Physiol. 32, 142–150. http://dx.doi.org/10.1159/000497475.

David, N.Ben., Richtman, Y., Gross, A., Ibrahim, R., Nyska, A., Ramot, Y., Mizrahi, B., 2023. Design and evaluation of dissolvable microneedles for treating atopic dermatitis. Pharmaceutics 15. http://dx.doi.org/10.3390/pharmaceutics15041109.

De Martino, S., Battisti, M., Napolitano, F., Palladino, A., Serpico, L., Amendola, E., Martone, A., De Girolamo, P., Squillace, A., Dardano, P., De Stefano, L., Dello Iacono, S., 2022. Effect of microneedles shape on skin penetration and transdermal drug administration. Biomater. Adv. (ISSN: 2772-9508) 142, 213169. http://dx.doi.org/10.1016/j.bioadv.2022.213169.

Donnelly, R.F., Garland, M.J., Morrow, D.I.J., Migalska, K., Singh, T.R.R., Majithiya, R., Woolfson, A.D., 2010. Optical coherence tomography is a valuable tool in the study of the effects of microneedle geometry on skin penetration characteristics and in-skin dissolution. J. Control. Release 147 (3), 333–341. http://dx.doi.org/10.1016/j.jconrel.2010.08.008.

Faridmehr, I., Osman, M., Adnan, A., Nejad, A., Hodjati, R., Amin, M., 2014. Correlation between engineering stress-strain and true stress-strain curve. Am. J. Civ. Eng. Archit. 2, 53–59. http://dx.doi.org/10.12691/ajcea-2-1-6.

Fung, Y., 1993. Biomechanics: Mechanical Properties of Living Tissues. New York, NY.

Gadamchetty, G., Pandey, A., Gawture, M., 2016. On practical implementation of the Ramberg–Osgood model for FE simulation. SAE Int. J. Mater. Manuf. 9, 200–205. http://dx.doi.org/10.4271/2015-01-9086.

Giardina, Jr., R., Wei, D., 2020. Ramberg–Osgood Material Behaviour Expression and Large Deflections of Euler Beams.

Goel, Vijay, Nyman, Jr., Edward, 2016. Computational modeling and finite element analysis. Spine 41, http://dx.doi.org/10.1097/BRS.0000000000001421, S6-S7.

González, D.G., 2016. A Continuum Mechanics Framework for Hyperelastic Materials: Connecting Experiments and Modelling (Doctoral dissertation). University Carlos III of Madrid.

Gubeljak, N., 2008. Application of Sintap to the Failure Assessment of Gas Pipes. http://dx.doi.org/10.1007/978-1-4020-6526-2_2.

Jagota, Vishal, Sethi, Amanpreet, Kumar, Dr-Khushmeet, 2013. Finite element method: An overview. Walailak J. Sci. Technol. 10, 1–8. http://dx.doi.org/10.2004/wjst.v10i1.499.

Jiang, L., Huang, Y., Pan, C., Ling, J., Li, J., Chen, Z., Fu, J., Wen, Y., 2016. Research on insertion process of medical needle. In: Proceedings of the ICMEMTC. pp. 779–785. http://dx.doi.org/10.2991/icmemtc-16.2016.154.

Khaniki, H.B., Ghayesh, M.H., Chin, R., et al., 2022. A review on the nonlinear dynamics of hyperelastic structures. Nonlinear Dynam. 110, 963–994. http://dx.doi.org/10.1007/s11071-022-07700-3.

Kim, N., 2015. Introduction to Nonlinear Finite Element Analysis. Springer, New York, NY, USA.

Kim, B., Lee, S.B., Lee, J., et al., 2012. A comparison among Neo-Hookean model, Mooney–Rivlin model, and Ogden model for chloroprene rubber. Int. J. Precis. Eng. Manuf. 13, 759–764. http://dx.doi.org/10.1007/s12541-012-0099-y.

Kong, X.Q., Zhou, P., Wu, C.W., 2011. Numerical simulation of microneedles' insertion into skin. Comput. Methods Biomech. Biomed. Eng. 14 (9), 827–835. http://dx.doi.org/10.1080/10255842.2010.497144.

Larrañeta, E., Lutton, R.E.M., Woolfson, A.D., Donnelly, R.F., 2016. Microneedle arrays as transdermal and intradermal drug delivery systems: Materials science, manufacture and commercial development. Mater. Sci. Eng. R 104, 1–32. http://dx.doi.org/10.1016/j.mser.2016.03.001.

Larrañeta, E., Moore, J., Vicente-Pérez, E.M., González-Vázquez, P., Lutton, R., Woolfson, A.D., Donnelly, R.F., 2014a. A proposed model membrane and test method for microneedle insertion studies. Int. J. Pharm. 472 (1–2), 65–73. http://dx.doi.org/10.1016/j.ijpharm.2014.05.042.

Larrañeta, E., Moore, J., Vicente-Pérez, E.M., González-Vázquez, P., Lutton, R., Woolfson, A.D., et al., 2014b. A proposed model membrane and test method for microneedle insertion studies. Int. J. Pharm. 472 (1–2), 65–73.

Liu, Tianqi, Sun, Yanfang, Zhang, Wenjing, Wang, Rui, Lv, Xinyu, Nie, Lei, Shavandi, Amin, Ergashovich, Yunusov, Jiang, Guohua, 2023. Mechanical investigation of solid MNs penetration into skin using finite element analysis. Adv. Eng. Mater. 26, http://dx.doi.org/10.1002/adem.202301532.

Loizidou, E.Z., Williams, N.A., Barrow, D.A., Eaton, M.J., McCrory, J., Evans, S.L., Allender, C.J., 2015. Structural characterisation and transdermal delivery studies on sugar microneedles: Experimental and finite element modelling analyses. Eur. J. Pharmaceut. Biopharmaceut. 89, 224–231.

Lutton, R.E.M., Larrañeta, E., Kearney, M.C., Boyd, P., Woolfson, A.D., Donnelly, R.F., 2015a. A novel scalable manufacturing process for the production of hydrogel-forming microneedle arrays. Int. J. Pharm. 494 (1), 417–429.

Lutton, R.E.M., Moore, J., Larrañeta, E., et al., 2015b. Microneedle characterisation: The need for universal acceptance criteria and GMP specifications when moving towards commercialisation. Drug Deliv. Trans. Res. 5, 313–331. http://dx.doi.org/10.1007/s13346-015-0237-z.

Makvandi, P., Kirkby, M., Hutton, A.R.J., Shabani, M., Yiu, C.K.Y., Baghbantaraghdari, Z., Jamaledin, R., Carlotti, M., Mazzolai, B., Mattoli, V., Donnelly, R.F., 2021a. Engineering microneedle patches for improved penetration: Analysis, skin models and factors affecting needle insertion. Nano-Micro Lett. 13 (1), 93. http://dx.doi.org/10.1007/s40820-021-00611-9, PMID: 34138349; PMCID: PMC8006208.

Makvandi, P., Kirkby, M., Hutton, A.R.J., Shabani, M., Yiu, C.K.Y., Baghbantaraghdari, Z., Jamaledin, R., Carlotti, M., Mazzolai, B., Mattoli, V., Donnelly, R.F., 2021b. Engineering microneedle patches for improved penetration: Analysis, skin models and factors affecting needle insertion. Nano-Micro Lett. 13, 93. http://dx.doi.org/10.1007/s40820-021-00611-9.

Marcé-Nogué, J., 2022. One step further in biomechanical models in palaeontology: A nonlinear finite element analysis review. PeerJ 10, 13890. http://dx.doi.org/10.7717/peerj.13890, PMID: 35966920; PMCID: PMC9373974.

Martins, P., Natal Jorge, R., Ferreira, A., 2006. A comparative study of several material models for prediction of hyperelastic properties: Application to silicone-rubber and soft tissues. Strain 42, 135–147.

McCrudden, M.T.C., Alkilani, A.Z., McCrudden, C.M., McAlister, E., McCarthy, H.O., Woolfson, A.D., Donnelly, R.F., 2014. Design and physicochemical characterisation of novel dissolving polymeric microneedle arrays for transdermal delivery of high dose, low molecular weight drugs. J. Control. Release 180, 71–80. http://dx.doi.org/10.1016/j.jconrel.2014.02.007.

McCrudden, M.T.C., Larrañeta, E., Clark, A., Jarrahian, C., Rein-Weston, A., Lachau-Durand, S., Niemeijer, N., Williams, P., Haeck, C., McCarthy, H.O., Zehrung, D., Donnelly, R.F., 2018. Design, formulation and evaluation of novel dissolving microarray patches containing a long-acting rilpivirine nanosuspension. J. Control. Release 292, 119–129. http://dx.doi.org/10.1016/j.jconrel.2018.11.002.

Melly, S., Liu, L., Liu, Y., Leng, J., 2021. A review on material models for isotropic hyperelasticity. Int. J. Mech. Syst. Dyn. 1, 71–88. http://dx.doi.org/10.1002/msd2.12013.

Meyer, W., 1996. Bemerkungen zur Eignung der Schweinehaut als biologisches Modell für die Haut des Menschen. Hautarzt 47, 178–182. http://dx.doi.org/10.1007/s001050050399.

Mohammed, D., Matts, P.J., Hadgraft, J., et al., 2012. Variation of stratum corneum biophysical and molecular properties with anatomic site. AAPS J. 14, 806–812. http://dx.doi.org/10.1208/s12248-012-9400-3.

Nasiri, M.I., Vora, L.K., Abu Ershaid, J., Peng, K., Tekko, I.A., Donnelly, R.F., 2022a. Nanoemulsion-based dissolving microneedle arrays for enhanced intradermal and transdermal delivery. Drug Deliv. Transl. Res. 12 (4), 881–896. http://dx.doi.org/10.1007/s13346-021-01107-0, PMCID: PMC8694761, PMID: 34939170.

Nasiri, M.I., Vora, L.K., Ershaid, J.A., et al., 2022b. Nanoemulsion-based dissolving microneedle arrays for enhanced intradermal and transdermal delivery. Drug Deliv. Transl. Res. 12, 881–896. http://dx.doi.org/10.1007/s13346-021-01107-0.

Özkaya, N., Leger, D., Goldsheyder, D., Nordin, M., 2017. Stress and strain. In: Fundamentals of Biomechanics. Springer, Cham, http://dx.doi.org/10.1007/978-3-319-44738-4_13.

Peng, K., Vora, L.K., Domínguez-Robles, J., Naser, Y.A., Li, M., Larrañeta, E., et al., 2021. Hydrogel-forming microneedles for rapid and efficient skin deposition of controlled release tip-implants. Mater. Sci. Eng. C 127, 112226.

Pissarenko, A., 2019. The materials science of skin: Analysis, characterisation, and modelling. Prog. Mater. Sci. 110, 100634. http://dx.doi.org/10.1016/j.pmatsci.2019.100634.

Pissarenko, A., Meyers, M.A., 2020. The materials science of skin: Analysis, characterization, and modeling. Prog. Mater. Sci. 110, 100634. http://dx.doi.org/10.1016/j.pmatsci.2019.100634.

R, W., Osgood, W.R., 1943. Description of Stress-Strain Curves By Three Parameters. National Advisory Committee for Aeronautics, Washington DC.

Ripolin, A., Quinn, J., Larrañeta, E., Vicente-Perez, E.M., Barry, J., Donnelly, R.F., 2017. Successful application of large microneedle patches by human volunteers. Int. J. Pharm. 521 (1–2), 92–101. http://dx.doi.org/10.1016/j.ijpharm.2017.02.011.

Salahshoori, Iman, Golriz, Mahdi, Nobre, Marcos A.L., Mahdavi, Shahla, Malekshah, Rahime Eshaghi, Javdani-Mallak, Afsaneh, Jorabchi, Majid Namayandeh, Khonakdar, Hossein Ali, Wang, Qilin, Mohammadi, Amir H., Mirnezami, Seyedeh Masoomeh Sadat, Kargaran, Farshad, 2024. Simulation-based approaches for drug delivery systems: Navigating advancements, opportunities, and challenges. J. Mol. Liq. (ISSN: 0167-7322) 395, 123888. http://dx.doi.org/10.1016/j.molliq.2023.123888.

Selvadurai, A.P.S., 2006. Deflections of a rubber membrane. J. Mech. Phys. Solids 54 (6), 1093–1119.

Senthil Murugan, S., Jegan, V., 2017. Development of hybrid composite for automobile application and its structural stability analysis using ANSYS. Int. J. Mod. Stud. Mech. Eng. (ISSN: 2454-9711) 3 (1), 23–34. http://dx.doi.org/10.20431/2454-9711.0301004, (Online).

Sliwoski, G., Kothiwale, S., Meiler, J., Lowe, Jr., E.W., 2013. Computational methods in drug discovery. Pharmacol. Rev. 66 (1), 334–395. http://dx.doi.org/10.1124/pr.112.007336, PMID: 24381236; PMCID: PMC3880464.

Tanaka, E., Miyawaki, Y., Del Pozo, R., Tanne, K., 2000. Changes in the biomechanical properties of the rat interparietal suture incident to continuous tensile force application. Arch. Oral. Biol. 45 (12), 1059–1064, 10.1016/S0003-9969(00)00082-0.

Tekko, I.A., Chen, G., Domínguez-Robles, J., Thakur, R.R.S., Hamdan, I.M.N., Vora, L., et al., 2020. Development and characterisation of novel poly (vinyl alcohol)/poly (vinyl pyrrolidone)-based hydrogel-forming microneedle arrays for enhanced and sustained transdermal delivery of methotrexate. Int. J. Pharm. 586, 119580.

Total Material, 2023. Retrieved from https://www.totalmateria.com/page.aspx?ID=CheckArticle&site=kts&NM=279.

Trotta, A., Ní Annaidh, A., 2019. Mechanical characterisation of human and porcine scalp tissue at dynamic strain rates. J. Mech. Behav. Biomed. Mater. (ISSN: 1751-6161) 100, 103381.

Vaucorbeil, A.de., Nguyen, VP., Sinaie, S., Wu, JY., 2020. Material point method after 25 years: Theory, implementation, and applications. In: Bordas, S.P.A., Balint, D.S. (Eds.), Advances in Applied Mechanics, Vol. 53. Elsevier, pp. 185–398. http://dx.doi.org/10.1016/bs.aams.2019.11.001.

Wei, J.C.J., Edwards, G.A., Martin, D.J., et al., 2017. Allometric scaling of skin thickness, elasticity, viscoelasticity to mass for micro-medical device translation: From mice, rats, rabbits, pigs to humans. Sci. Rep. 7, 15885. http://dx.doi.org/10.1038/s41598-017-15830-7.

Wu, Y., Vora, L.K., Donnelly, R.F., et al., 2023a. Rapidly dissolving bilayer microneedles enabling minimally invasive and efficient protein delivery to the posterior segment of the eye. Drug Deliv. Transl. Res. 13, 2142–2158. http://dx.doi.org/10.1007/s13346-022-01190-x.

Wu, W., Xia, R., Qian, G., Liu, Z., Razavi, N., Berto, F., Gao, H., 2023b. Mechanostructures: Rational mechanical design, fabrication, performance evaluation, and industrial application of advanced structures. Prog. Mater. Sci. (ISSN: 0079-6425) 131, 101021. http://dx.doi.org/10.1016/j.pmatsci.2022.101021.

Xiao, M., Wang, Z., An, Y., Dai, Y., Wang, X., Zhu, Z., 2024. Fabrication and mechanical modelling of dissolvable PVA/PVP composite microneedles with biocompatibility for efficient transdermal delivery of ibuprofen. J. Biomater. Sci. Polym. Ed. 35 (9), 1439–1454. http://dx.doi.org/10.1080/09205063.2024.2333627.

Xiu, X., Gao, G., Liu, Y., Ma, F., 2022. Drug delivery with dissolving microneedles: Skin puncture, its influencing factors and improvement strategies. J. Drug. Deliv. Sci. Technol. 76, 103653. http://dx.doi.org/10.1016/j.jddst.2022.103653.

Yadav, P.R., Han, T., Olatunji, O., Pattanayek, S.K., D.B., Das, 2020. Mathematical modelling, simulation and optimisation of microneedles for transdermal drug delivery: Trends and progress. Pharmaceutics 12 (8), 693. http://dx.doi.org/10.3390/pharmaceutics12080693, PMID: 32707878; PMCID: PMC7464833.

Yadav, P.R., Nasiri, M.I., Vora, L.K., Larrañeta, E., Donnelly, R.F., Pattanayek, S.K., Das, D.B., 2022. Super-swelling hydrogel-forming microneedle based transdermal drug delivery: Mathematical modelling, simulation and experimental validation. Int. J. Pharm. 622, 121835. http://dx.doi.org/10.1016/j.ijpharm.2022.121835.

Yan, Q., Weng, J., Shen, S., Wang, Y., Fang, M., Zheng, G., Yang, Q., Yang, G., 2021. Finite element analysis for biodegradable dissolving microneedle materials on skin puncture and mechanical performance evaluation. College of Pharmaceutical Sciences, Zhejiang University of Technology, Hangzhou, China. Polymers 13 (18), 3043.